

ON ESTIMATION OF CONTAMINATION FROM HYDROGEN CYANIDE IN CARBON MONOXIDE LINE-INTENSITY MAPPING

DONGWOO T. CHUNG¹, TONY Y. LI¹, MARCO P. VIERO¹, SARAH E. CHURCH¹, AND RISA H. WECHSLER^{1,2}

¹Kavli Institute for Particle Astrophysics and Cosmology; Physics Department, Stanford University, Stanford, CA 94305, USA; dongwooc@stanford.edu

²SLAC National Accelerator Laboratory, Menlo Park, CA 94025, USA

ABSTRACT

Line-intensity mapping surveys probe large-scale structure through spatial variations in molecular line emission from a population of unresolved cosmological sources. Future such surveys of carbon monoxide line emission, specifically the CO(1-0) line, face potential contamination from a disjoint population of sources emitting in a hydrogen cyanide emission line, HCN(1-0). This paper explores the potential range of the strength of HCN emission and its effect on the CO auto power spectrum, using simulations with an empirical model of the CO/HCN–halo connection. We find that effects on the observed CO power spectrum depend on modeling assumptions but are very small for our fiducial model, which is based on current understanding of the galaxy–halo connection. Given the fiducial model, we expect the bias in overall CO detection significance due to HCN to be less than 1%.

Keywords: galaxies: high-redshift — galaxies: statistics — radio lines: galaxies

1. INTRODUCTION

Line-intensity mapping is a novel method of mapping large-scale structure in the early universe through space and time, in which broad spatial variations in line-intensity throughout the surveyed volume trace galaxies too faint to be resolved individually in a conventional galaxy survey. Such observations allow for a statistical understanding of a large population of galaxies, without resolving every galaxy individually. The spectral lines that these surveys target arise from certain species of molecular gas abundant in these galaxies, generally connected to star-formation activity. Therefore, line-intensity mapping can contribute to our understanding of the history of galaxy formation and reionization, as well to our understanding of the evolution of large-scale structure in our universe (Chang et al. 2010; Visbal & Loeb 2010; Gong et al. 2011; Pullen et al. 2013; Uzgil et al. 2014; Breyse et al. 2016; Li et al. 2016).

Line-intensity surveys have a host of foregrounds and systematics, but a foreground of primary concern is emission from spectral lines other than the line of interest. Removal of this foreground presents a challenge not present in some other foregrounds, like dust or CMB emission, which are spectrally smooth across the observed frequency band. Foreground line emission, on the other hand, has sharp, structured variations in intensity, as we would expect from any spectral line.

Here, we explore the effect of line emission contamination specifically in the context of the initial phase of the Carbon monOxide Mapping Array Pathfinder (COMAP), an experiment that is in development to map carbon monoxide (CO) line emission in CO(1-0) (rest frequency 115.26 GHz) at redshift $z \approx 2.4$ –3.4 (see Table 1 for details). We expect the COMAP results to complement those of the interferomet-

ric CO Power Spectrum Survey (COPSS; see Keating et al. 2016).

We expect one of the brightest contaminant lines for COMAP and other CO(1-0) surveys to be a hydrogen cyanide (HCN) line, HCN(1-0), with a rest frequency of 88.63 GHz (Breyse et al. 2015). CO emission from a redshift range of $z \approx 2.4$ –3.4, as targeted by COPSS and COMAP, mixes with HCN emission from $z \approx 1.6$ –2.4. In attempting to understand the effect of such contamination on CO observations, we consider in this work:

- What intensities are expected from HCN emission?
- To what extent do we estimate HCN emission would bias the CO auto power spectrum?
- How do uncertainties in modelling line emission affect predictions of HCN contamination in a CO survey?

This work is not the first to ask some of these questions. Indeed, it follows the works of Breyse et al. (2015) and Visbal et al. (2011) on line foregrounds. However, here we incorporate the methods of Li et al. (2016) to estimate the CO signal and HCN contamination. We derive line-luminosity relations from star-formation histories in cosmological simulations and observations of many local galaxies¹. Furthermore, as in Li et al. (2016), we use halo catalogues from dark matter simulations rather than analytically derived galaxy distributions as in Breyse et al. (2015). This approach affords greater flexibility in generating mock galaxies and sky data

¹ Visbal et al. (2011) calibrate many of their line-luminosity relations solely based on M82, and do not examine HCN(1-0). In addition, their focus was on CO(1-0)–CO(2-1) cross-correlation.

Table 1. COMAP instrumental and survey parameters assumed for this work.

Parameter	Value
System temperature	44 K
Angular resolution	4'
Frequency resolution	40 MHz
Observed frequencies	26–30 GHz 30–34 GHz
Number of feeds	19
Survey area per patch	2.5 deg ²
On-sky time per patch	1500 hours

NOTE—Feeds are single-polarization. The survey will cover a total range of 26–34 GHz in frequency, but with two separate downconverter systems each covering a 4 GHz band in that range. The angular resolution above is the full width at half maximum of the Gaussian beam profile, for the receiver’s central pixel.

in preparation for COMAP, while requiring fewer simplifying assumptions about galaxy clustering. Our work is thus novel in the sum of its methodology and objectives, and continues a larger exploration of synthetic COMAP observations that began with Li et al. (2016).

The paper is structured as follows: in Section 2 we introduce our methods for simulating CO observations and HCN contamination in these observations, and how we can vary those methods. We then present expected contamination in observed intensity and in power spectra in Section 3, with some considerations of impact on detection significance of the reduced data. After some discussion of these results and their implications for COMAP and other future CO surveys in Section 4, we present our conclusions in Section 5.

Where necessary, we assume base-10 logarithms, and a Λ CDM cosmology with parameters $\Omega_m = 0.286$, $\Omega_\Lambda = 0.714$, $\Omega_b = 0.047$, $h = 0.7$, $\sigma_8 = 0.82$, and $n_s = 0.96$.

2. METHODS

The methods and results of Li et al. (2016) form the basis for this study. In short, we model and apply the galaxy–halo connection to dark matter halos identified in a cosmological N-body simulation. Through a chain of empirical relations, we assign galaxy line-luminosities to individual halos, and use these luminosities to generate simulated data and power spectra. We summarise this part of our methodology in Section 2.2 and Section 2.3, but first in Section 2.1 we compare the scope of this work to that of previous work with similar methods and aims.

2.1. Context in previous work

The work of Breyse et al. (2015) considers line foregrounds in the context of hypothetical CO, [CII], and Ly- α intensity surveys, and proposes that mitigation of these foregrounds in a CO survey is feasible by masking the brightest parts of the map. To motivate this mitigation, Breyse

et al. (2015) show that HCN significantly contaminates simulated CO surveys, with the HCN power spectrum sitting near or above the CO spectrum. However, the authors use an assumed galaxy power spectrum to simulate an intensity map with the expected clustering, rather than a cosmological simulation. The work in Breyse et al. (2015) is also limited to HCN contamination (and its mitigation) in 2D maps, for a single observed frequency channel. We must then ask whether high contamination in data products from 2D maps translates to equally high contamination in data products from a 3D cube, the latter of which is our concern. That question is a primary motivation for this work, and our results ultimately do demonstrate similar contamination in both 2D and 3D maps, but not necessarily contamination at the level claimed in Breyse et al. (2015).

As we will discuss in the following sections, the simulations of Li et al. (2016) incorporate complications not present in the simulations of Breyse et al. (2015). While the results of Li et al. (2016) show promising prospects for detection of the CO auto spectrum and meaningful constraints on properties of galaxy populations, our work now adds potential effects of HCN contamination as forecast by Breyse et al. (2015).

2.2. Simulated observations

In Section 2.2.1, we describe the dark matter simulation used to generate the halos in our observation volume, and in Section 2.2.2 and Section 2.2.4, we outline the procedure used to generate simulated temperature cubes with these halos.

2.2.1. Dark matter simulation

We use the cosmological N-body simulation `c400–2048` described in Li et al. (2016), which provides implementation details of the simulation and subsequent halo identification. The simulation has a dark matter particle mass of $5.9 \times 10^8 M_\odot h^{-1}$, and we include dark matter halos more massive than $M_{\text{vir}} = 10^{10} M_\odot$ in our analysis. We will address this mass cutoff further in Section 2.2.2 and Section 2.2.3.

To simulate galaxies in our field of observation, we use dark matter halos identified in “lightcone” volumes, enclosing all halos within a given sky area and redshift range, with each lightcone based on arbitrary choices of observer origin and direction within the cosmological simulation. We use 100 $z = 2.3$ – 2.9 and 100 $z = 1.5$ – 2.0 lightcones populated with $\sim 10^6$ – 10^7 halos over a flat-sky area of $100' \times 100'$. Random pairings of these lightcones form the basis for our simulated observations.

2.2.2. Halo mass–line-luminosity relation

We assign each halo a luminosity in each line based on its sky position, mass, and cosmological redshift (excluding peculiar velocities). We first consider a fiducial model (the ‘turnaround model’) that builds on previous work in Li et al. (2016), and then consider variations on this model in the following section.

Fiducial model— The ladder of relations used in Li et al. (2016) to convert halo masses to CO line-luminosity is as follows.

- Assume only halos above a cutoff mass of $10^{10} M_{\odot}$ can support emission in any line, and assign zero luminosity to halos below this mass.
- Convert halo masses to star-formation rates (SFR) for each halo via interpolation of data from Behroozi et al. (2013a) and Behroozi et al. (2013b). The main focus of these papers is to constrain the stellar mass–halo mass relation and derived quantities such as SFR by comparing simulation data with observational constraints, and the resulting data include average SFR in a halo given its mass and redshift. This relation shows a peak in SFR around $10^{11.7} M_{\odot}$ on average, beyond which star-formation efficiency appears to fall off. This turnaround in the relation is consistent with previous analyses, as Behroozi et al. (2013a) note.
- Approximate halo-to-halo scatter in SFR by adding 0.3 dex log-normal scatter to the SFR obtained above, preserving the linear mean.
- Convert SFR into infrared (IR) luminosity, using a known tight correlation:

$$\frac{\text{SFR}}{M_{\odot} \text{ yr}^{-1}} = \delta_{\text{MF}} \times 10^{-10} \left(\frac{L_{\text{IR}}}{L_{\odot}} \right). \quad (1)$$

As in Behroozi et al. (2013a) and Li et al. (2016), we take $\delta_{\text{MF}} = 1.0$, corresponding to a Chabrier initial mass function (IMF). We note the uncertainty of this relation in low-mass halos, where dust obscuration may not completely cover star-formation activity (Wu & Doré 2017).

- Convert between IR luminosity and observed CO luminosity through power-law fits to observed data, commonly given in the literature:

$$\log \left(\frac{L_{\text{IR}}}{L_{\odot}} \right) = \alpha \log \left(\frac{L'_{\text{CO}}}{\text{K km s}^{-1} \text{ pc}^2} \right) + \beta, \quad (2)$$

where for our fiducial model, we take $\alpha = 1.37$ and $\beta = -1.74$ from a fit to high-redshift galaxy data ($z \gtrsim 1$) given in Carilli & Walter (2013), following Li et al. (2016).

- Add 0.3 dex log-normal scatter in CO luminosity, again preserving the linear mean.

In general, to convert halo masses to *any* line-luminosity that correlates reasonably tightly with IR luminosity, we simply need a relation of the form

$$\log \left(\frac{L_{\text{IR}}}{L_{\odot}} \right) = \alpha \log \left(\frac{L'_{\text{line}}}{\text{K km s}^{-1} \text{ pc}^2} \right) + \beta. \quad (3)$$

Gao & Solomon (2004), based on a mixed sample of normal galaxies and luminous and ultra-luminous infrared galaxies (LIRGs and ULIRGs, $z < 0.06$), obtain $\alpha = 1.00 \pm 0.05$ and $\beta = 2.9$ for HCN(1-0). Since $\alpha = 1$, this relation between IR and HCN luminosity is linear.

L'_{line} is the observed luminosity (or velocity- and area-integrated brightness temperature) of the halo, which we convert into an intrinsic luminosity for each halo, as in Li et al. (2016):

$$\frac{L_{\text{line}}}{L_{\odot}} = 4.9 \times 10^{-5} \left(\frac{\nu_{\text{line,rest}}}{115.27 \text{ GHz}} \right)^3 \frac{L'_{\text{line}}}{\text{K km s}^{-1} \text{ pc}^2}. \quad (4)$$

Note that while this relation is taken from a CO model, it is actually a re-statement of

$$L_{\text{line}} = \frac{8\pi k_B}{c^3} \nu_{\text{line,rest}}^3 L'_{\text{line}}, \quad (5)$$

which arises from general definitions of the two luminosity quantities in the Rayleigh–Jeans approximation, which we still apply for HCN line emission.²

In simulating halo-to-halo scatter in the line-luminosity itself, we add 0.3 dex log-normal scatter to both CO and HCN line-luminosities in the IR–line-luminosity relation. In both lines, the amount of scatter is consistent with the amount of scatter present in the local observations forming the basis for our scaling relations. Whether this scatter accurately reflects fluctuations in star-formation activity in individual galaxies is an outstanding question, but we will at least attempt to address how our results depend on the amount of scatter in the following sections.

2.2.3. Model variations

We introduce a few variations on the fiducial model, in order to address potential concerns:

- Various papers since Gao & Solomon (2004) have carried out re-analyses of the same data with small additional samples (mostly at $z \ll 1$, but also a handful of detections at $z \gtrsim 1$). The re-analyses in Carilli et al. (2005) and García-Burillo et al. (2012) show the IR–HCN correlation to be at least marginally non-linear, respectively with best-fit parameters of $(\alpha, \beta) = (1.09 \pm 0.02, 2.0)$ and $(\alpha, \beta) = (1.23 \pm 0.05, 1.07 \mp 0.40)$. Since we assume the linear relation from Gao & Solomon (2004), we should understand how our estimates of contamination vary with the mean IR–HCN relation.
- The scatter we introduce in SFR and in HCN luminosity is shorthand for variations in star-formation activity and gas dynamics in individual halos. The fiducial values we assume are based on local observations, and cosmic trends in such dynamical activity may result in greater halo-to-halo scatter at some redshifts than at others. We thus explore how our estimates of contamination vary with increased scatter in HCN luminosity.
- In their work, Breyse et al. (2015) use a single power-law relation to assign luminosities to halos, very unlike our fiducial model which introduces a downturn

² Emission in CO(1-0) and HCN(1-0) is not technically in the Rayleigh–Jeans regime, but the historical convention in radio astronomy is to report brightness temperature in this approximation, where ‘temperature’ scales linearly with surface brightness (Carilli & Walter 2013). We continue to use this convention, which allows for easier comparison not only with previous literature, but with instrument sensitivity.

at high masses. We must explore how this simplified form of the halo mass–SFR relation affects our estimates of HCN contamination.

The mean $L_{\text{IR}}-L'_{\text{HCN}}$ relation— For this paper, we simply generate additional halo luminosities for each lightcone, based on the alternate α and β from the two re-analyses mentioned above. These alternate values do not vary by more than a factor of order unity from the values given in Gao & Solomon (2004). We may not expect this level of variation to make much difference in the HCN power spectrum, especially relative to CO. We will quantitatively show in Section 3.1, Section 3.2, and Section 3.3 that indeed, such variation makes little difference in the HCN temperatures and CO spectrum contamination, especially compared to the other model variations listed here.

Gao & Solomon (2004) also suggest a strong CO–HCN correlation in luminosity, based on a fit of HCN luminosities to both CO and far-IR luminosities. Again, given that the above variations in determining HCN luminosity make little difference, we omit consideration of CO-dependence for simplicity.

Halo-to-halo scatter in line-luminosity— We have no reason to suspect significant cosmic evolution of scatter in luminosities with redshift based on observational data. Sun et al. (2016) also study line emission contamination in line-intensity mapping (in the context of the Tomographic Ionised-carbon Mapping Experiment, or TIME, designed to map [CII] emission at $z \sim 6.5$), and mitigation through masking brighter foreground galaxies. As part of this work, that paper characterises the halo mass– L_{IR} relation, and sees no obvious evolution of scatter in L_{IR} with redshift up to $z \sim 1.5$.

However, we should still explore the possibility that scatter in the $L_{\text{IR}}-L'_{\text{line}}$ relation *does* vary over redshift or across different gas species. We vary the HCN luminosity scatter between 0.0 dex, 0.3 dex, 0.5 dex, and 1.0 dex. Of these, 0.3 dex is the fiducial value, and the value used with the turnaround model unless otherwise specified. Note that we keep the SFR scatter at 0.3 dex in all simulations.

The form of the halo mass–SFR relation— The power-law model of Breyse et al. (2015) follows Pullen et al. (2013), which in part investigates cross-correlation prospects between CO line emission and samples of quasi-stellar objects (QSO). The model is as follows:

- Select a fraction of halos to emit in each line, based on the assumption of a duty cycle for emission. The model assumes that the duty cycle of star-formation and thus line emission is given by

$$f_{\text{duty}} = t_s / t_{\text{age}}(z), \quad (6)$$

where $t_s \sim 10^8$ years is the approximate time-scale of star-formation, and $t_{\text{age}}(z)$ the age of the universe in our redshift range. While the duty cycle thus evolves with redshift, we take a constant f_{duty} for each lightcone, using the average age of the universe over the applicable redshift range.

Table 2. Summary of HCN models explored in this paper.

Model	Description
turnaround	based on Li et al. (2016) <ul style="list-style-type: none"> • SFR from Behroozi et al. (2013a) relation (peaks at halo masses of $\sim 10^{12} M_{\odot}$) • log-normal scatter in SFR of 0.3 dex • SFR scaled to L_{IR} assuming IMF • $L_{\text{IR}}-L_{\text{HCN}}$ scaling from Gao & Solomon (2004) • scatter in L_{HCN} of 0.0, 0.3, 0.5, or 1.0 dex
power-law	based on Breyse et al. (2015) <ul style="list-style-type: none"> • $L_{\text{HCN}}/L_{\odot} = A(M/M_{\odot})^b$ • only f_{duty} of halos emit in HCN <i>alternatively:</i> <ul style="list-style-type: none"> • $L_{\text{HCN}}/L_{\odot} = f_{\text{duty}}A(M/M_{\odot})^b$ • all halos emit in HCN line

NOTE—The fiducial model parameters are indicated in bold. In all cases, there is a cutoff mass below which halos do not host HCN emitters, and that mass is $10^{10} M_{\odot}$ in this paper for all models.

- For those halos that do emit, the halo mass–line-luminosity relation per halo is a simple power law with empirically constrained parameters:

$$\frac{L_{\text{line}}}{L_{\odot}} = A \left(\frac{M}{M_{\odot}} \right)^b, \quad (7)$$

where for CO, Breyse et al. (2015) use $A = 2 \times 10^{-6}$ and $b = 1$ following Pullen et al. (2013) (originally from Wang et al. 2010), and for HCN use $A = 1.7 \times 10^{-15}$ and $b = 1.67$ as derived from Gao & Solomon (2004).

Given $t_s = 100$ Myr as assumed in past literature, $f_{\text{duty}} \approx 2.5\%$ for the HCN lightcones and $\approx 4\%$ for the CO lightcones. However, observations at $z \sim 1-3$ suggest a near-unity duty cycle (Daddi et al. 2007; Noeske et al. 2007; Keating et al. 2016). Therefore, we use two power-law models with different uses of f_{duty} . One model follows Breyse et al. (2015) closely, selecting f_{duty} of halos above the cutoff mass to emit with luminosity $A(M/M_{\odot})^b L_{\odot}$. In the other model, we assume a duty cycle of unity and absorb f_{duty} into the luminosity calculation, so that all halos above the cutoff mass emit with luminosity $f_{\text{duty}}A(M/M_{\odot})^b L_{\odot}$.

Our fiducial model HCN relation is based on the same IR–HCN luminosity relation that Breyse et al. (2015) use. The CO relation used for the fiducial model does differ from that used for the power-law models and in Breyse et al. (2015), but we use those values for our power-law models to compare our results more easily with Breyse et al. (2015). Broadly speaking, α (or $(5/3)b^{-1}$) for CO is still significantly higher than α for HCN, resulting in lower-mass halos contributing more in CO emission than in HCN emission.

Figure 1 shows the mean halo mass–line-luminosity relations at the redshifts for CO and HCN corresponding to the midpoint of the COMAP 30–34 GHz band. Due to the turnaround in the halo mass–SFR relation from Behroozi

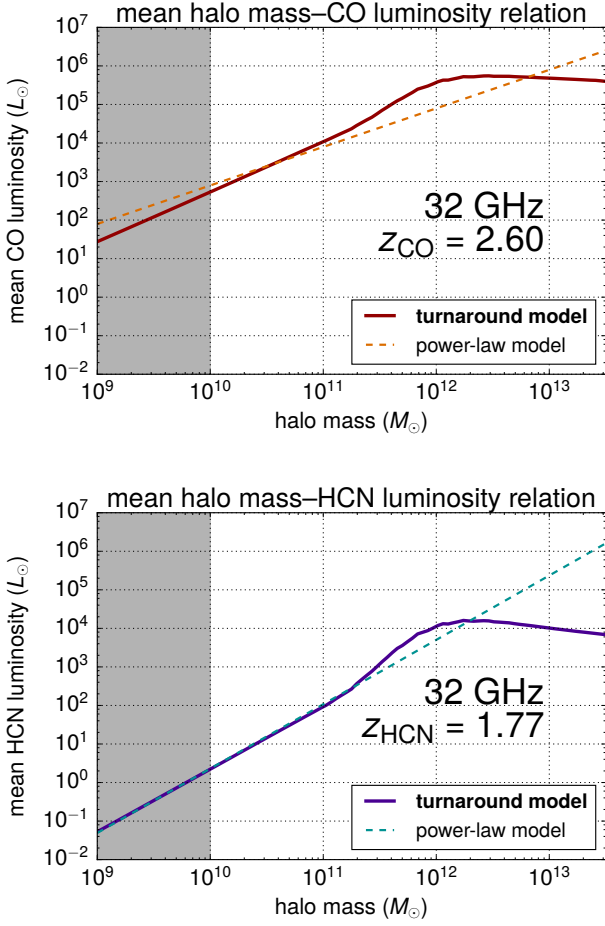


Figure 1. Mean relations for halo mass–CO luminosity at $z = 2.60$ (**upper panel**) and halo mass–HCN luminosity at $z = 1.77$ (**lower panel**), used in this work and in Breyse et al. (2015). The redshifts correspond to an observed frequency of 32 GHz for each line. Simulations assign luminosities with halo-to-halo scatter not depicted in this figure. For the power-law model, the relations plotted include the factor of f_{duty} for CO and HCN. The grey area in each panel indicates halo masses excluded from emitting at all in this work and in Li et al. (2016), but not in Breyse et al. (2015).

et al. (2013a), the average line-luminosity for halos of mass $\gtrsim 10^{12} M_{\odot}$ is substantially lower in our fiducial model than in either power-law model, especially for HCN. We expect that the lower luminosities are more realistic, based on (a) the clear constraints on the shape of the stellar mass–halo mass relationship in Behroozi et al. (2013a) and (b) comparisons with existing HCN observations in Appendix A.

Simulations with our power-law models still diverge in important details from Breyse et al. (2015). We use simulated dark matter halos in 3D rather than generating 2D maps to fit expected power spectra. The particle mass of our dark matter simulation ($\sim 10^9 M_{\odot}$) limits the mass-completeness of our halo catalogues, so we continue to use a cutoff mass for emission of $10^{10} M_{\odot}$, rather than the cutoff mass in Breyse et al. (2015) of $10^9 M_{\odot}$. So we treat these power-law models as a variation of the form of the halo mass–SFR relation, not an attempt to replicate the results of Breyse et al. (2015).

A lower cutoff mass cuts out a potential population of faint

emitters, impacting the signal and contaminant forecasts (and we will return to this point in Section 3.1 and Section 4.1.2). That said, the impact would not be at the scale of orders of magnitude. Take the average map temperature as a zeroth-order metric of signal intensity. Li et al. (2016) (in Appendix A.1 of that paper) make an analytic calculation of $\langle T_{\text{CO}} \rangle$ as a function of the minimum CO-emitting halo mass, based on the fiducial halo mass–CO luminosity scaling relations and an assumed halo mass function (not subject to completeness concerns). Through this calculation, they show that moving the cutoff mass down to $10^9 M_{\odot}$ would not have significantly impacted their mean CO brightness temperature $\langle T_{\text{CO}} \rangle$ for the fiducial model. Since HCN luminosity falls even faster with decreasing halo mass (see Figure 1), we expect changes in cutoff mass to affect HCN even less.

For easy reference, we recap the fiducial and power-law models in Table 2.

2.2.4. Halo luminosities to observations

Table 1 gives the instrumental and survey parameters anticipated for the initial phase of COMAP. We use these parameters to generate a data cube from the halo luminosities assigned within the lightcone.

Each volume element (voxel) in the data cube has angular widths δ_x and δ_y and frequency resolution δ_{ν} . Here, $\delta_x = \delta_y = 0.6'$, while $\delta_{\nu} = 40 \text{ MHz}$.³ (Following changes in COMAP design during the preparation of this work, we now expect the actual experiment to take data with $\delta_{\nu} \approx 10 \text{ MHz}$.) Since the sky grid is an order of magnitude finer than the stated angular resolution of the actual survey, the simulated maps retain modes on spatial scales smaller than would be observable in reality. This should not affect any conclusions we draw about the level of contamination that HCN emission would contribute to the CO signal.

We follow Li et al. (2016) again in generating a temperature cube:

- Bin the halo luminosities into resolution elements in frequency and angular position, resulting in a certain luminosity associated with each voxel.
- Convert these luminosities into surface brightness (apparent spectral intensity, in units of luminosity per unit area, per unit frequency, per unit solid angle):

$$I_{\nu, \text{obs}} = \frac{L_{\text{line}}}{4\pi D_L^2} \frac{1}{\delta_x \delta_y \delta_{\nu}}. \quad (8)$$

- Convert to the expected brightness temperature contribution from each voxel. The Rayleigh–Jeans brightness temperature for a given surface brightness is

$$T = \frac{c^2 I_{\nu, \text{obs}}}{2k_B \nu_{\text{obs}}^2}, \quad (9)$$

from which we obtain our temperature for each voxel in the data cube.

³ This corresponds to a comoving voxel of roughly $1.1 \times 1.1 \times 4.6 \text{ cMpc}^3$ at redshift 2.60, or $0.86 \times 0.86 \times 5.6 \text{ cMpc}^3$ at redshift 1.77.

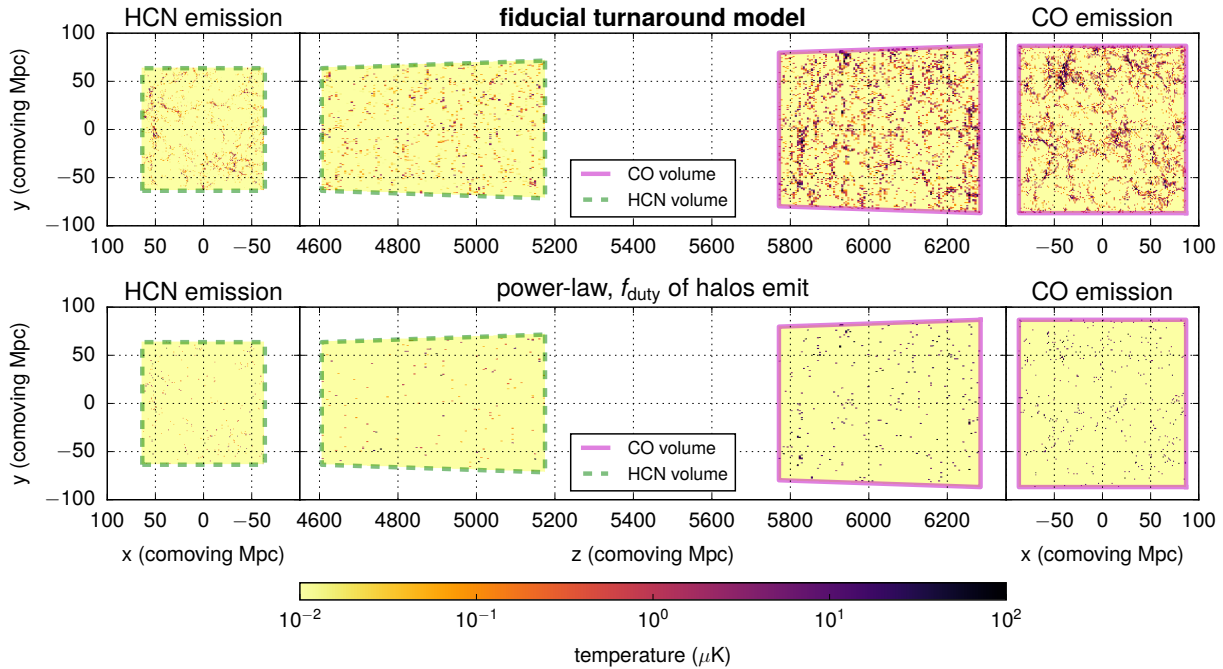


Figure 2. Sample slices from temperature cubes generated with the fiducial model (**upper panels**) and a power-law model (**lower panels**), projected into comoving space. The underlying halos are the same. **Left panels:** a slice of the HCN temperature cube, in transverse (on-sky) directions. **Middle panels:** slices of the HCN and CO temperature cubes, with one axis along the line of sight. Note the difference in comoving volume and location. **Right panels:** a slice of the CO temperature cube, again in transverse directions.

At the time of writing, we do not have a clear idea of what each COMAP sky patch will look like, so we simulate an observation over a square $95' \times 95'$ patch in a 30–34 GHz frequency band (corresponding to our choice of lightcones covering $z = 2.3$ – 2.9 and $z = 1.5$ – 2.0). Note that during the preparation of this work, COMAP expanded its instrument bandwidth to cover 26–30 GHz as well. We do not expect such differences from the actual survey, or the omission of various systematics and cosmological effects, to radically affect our conclusions.

For a given pair of lightcones, we simulate CO and HCN temperature data in the same observed sky and frequency bins, and then add them together to simulate a CO observation with HCN contamination. This addresses any concerns discussed in Breyse et al. (2015) that arise from projecting power spectra from a lower-redshift region into a higher-redshift region. Figure 2 depicts the difference in the comoving volumes observed in CO(1-0) versus in HCN(1-0) by the same survey.

2.3. Power spectra from observations

We work with the spherically averaged, comoving 3D power spectrum $P(k)$, and the average of all 2D sky angular power spectra C_ℓ from each frequency channel in the data cube. We calculate $P(k)$ by calculating the full 3D power spectrum $P(\mathbf{k})$ of the temperature cube in comoving space, binning it in radial ‘shells’ of $k = |\mathbf{k}|$, and averaging the full spectrum in each bin. We obtain C_ℓ in each frequency channel through similar binning of the 2D power spectrum in \mathbf{k} -space. As Figure 2 shows, the comoving volume is not perfectly rectangular, but we approximate it as such for $P(k)$ cal-

culations here.

As in Li et al. (2016) and Breyse et al. (2015), we present the spherical 3D power spectra as $\Delta^2(k) = k^3 P(k)/(2\pi^2)$, and the averaged 2D power spectra in the conventional C_ℓ form, using a flat-sky approximation as in Chiang & Chen (2012) and Breyse et al. (2015). While the 3D analogue to C_ℓ is just $P(k)$ rather than the rescaled $\Delta^2(k)$, and the 2D analogue to $\Delta^2(k)$ is the suitably rescaled $\ell(\ell+1)C_\ell/(2\pi)$ rather than just C_ℓ , we use these rather disparate presentations to follow the conventions used in previous literature.

3. RESULTS

3.1. Simulated temperature cubes

For 496 different pairs of CO and HCN lightcones, we generate temperature cubes for CO emission and HCN emission, which we then add together in observed voxels to obtain a simulated map for CO emission plus HCN contamination. Approximately 1.5×10^6 halos in the CO lightcones and approximately 5.4×10^6 halos in the HCN lightcones typically fall above the cutoff mass of $10^{10} M_\odot$ and within a $95' \times 95'$ patch. Since we used only 100 lightcones populated with CO emitters and 100 lightcones populated with HCN emitters, there is some redundancy in the lightcones used. But since temperature maps were generated anew for each new pairing, even two maps from the same lightcone are subject to some differences due to re-application of halo-to-halo scatter in SFR and luminosity. On top of the halo-to-halo scatter in each lightcone, sample variance in large-scale structure between lightcones results in lightcone-to-lightcone scatter in temperature and power spectra.

Figure 2 shows slices of a sample pair of temperature data

Table 3. Median and 95% sample interval of mean brightness temperature in each line over the survey volume, in simulated observations of all 496 lightcone pairs.

Model description	$\sigma_{L_{\text{HCN}}}$ (dex)	$\langle T_{\text{CO}} \rangle$ (μK)	$\langle T_{\text{HCN}} \rangle$ (μK)
	0.0	$0.904^{+0.125}_{-0.100}$	$0.062^{+0.009}_{-0.007}$
turnaround model: non-power-law $M_{\text{halo}}-L_{\text{line}}$ relations, with log-normal scatter	0.3	$0.906^{+0.124}_{-0.102}$	$0.062^{+0.009}_{-0.007}$
	0.5	$0.906^{+0.120}_{-0.101}$	$0.062^{+0.009}_{-0.007}$
	1.0	$0.905^{+0.121}_{-0.102}$	$0.060^{+0.015}_{-0.009}$
power-law model, f_{duty} of halos with $M_{\text{h}} > 10^{10} M_{\odot}$ emit at $L_{\text{line}} = A(M/M_{\odot})^{\beta} L_{\odot}$	n/a	$0.471^{+0.064}_{-0.053}$	$0.137^{+0.121}_{-0.050}$
power-law model, all halos with $M_{\text{h}} > 10^{10} M_{\odot}$ emit at $L_{\text{line}} = f_{\text{duty}} A(M/M_{\odot})^{\beta} L_{\odot}$	n/a	$0.470^{+0.062}_{-0.052}$	$0.146^{+0.044}_{-0.035}$

NOTE—The fiducial model parameters are indicated in bold. See Section 2.2.2 for details of each model. $\sigma_{L_{\text{HCN}}}$ does not include log-normal scatter in SFR, and is not an applicable parameter for the power-law models.

cubes for a given pair of lightcones. Note that these slices are generated with the fiducial model (the turnaround model with 0.3 dex log-scatter in luminosity). The power-law model maps appear much sparser than maps from any of the other models, especially when only f_{duty} of sufficiently massive halo host emitters.

Table 3 lists the mean line temperatures over each simulated CO map and HCN map. Variations in $\sigma_{L_{\text{HCN}}}$ do not appear to significantly affect $\langle T_{\text{HCN}} \rangle$, and any differences present could be ascribed to map-to-map scatter. The power-law models yield lower mean CO temperatures by approximately a factor of 2 in comparison to the fiducial model results, but also higher HCN mean temperatures by approximately a factor of 2. We might expect the slight change in the choice of empirical IR–line–luminosity relation to change the CO temperature, but there is no such change for HCN.

We can compare these cube temperatures to analytic calculations based on the line–luminosity per volume $dL_{\text{line}}/dV = \int L_{\text{line}}(M)(dn/dM)dM$, where dn/dM is the halo mass function fit in Behroozi et al. (2013b) adapted to the appropriate redshifts (at the midpoint of the simulated observing band) and cosmology. The $L_{\text{line}}(M)$ function used here is an average across all halos of mass M , and thus absorbs any factors of f_{duty} . Those calculations predict $\langle T_{\text{CO}} \rangle = 0.888 \mu\text{K}$ and $\langle T_{\text{HCN}} \rangle = 0.058 \mu\text{K}$ for the fiducial model, versus $\langle T_{\text{CO}} \rangle = 0.459 \mu\text{K}$ and $\langle T_{\text{HCN}} \rangle = 0.125 \mu\text{K}$ for the power-law model. All of these temperatures are consistent with the range of empirically obtained brightness temperatures in Table 3. This analytic calculation also allows us to estimate the contribution to the brightness temperature from different bins of halo masses. We quantify this in Figure 3 using a slight variation on the integrand, $L_{\text{line}}(M)dn/d(\log M)$.

As a prelude to the discussion of power spectra in the next section, we also provide an analytic illustration of how different bins of halo masses contribute to the shot noise component of the power spectrum. To illustrate the contribution to mean line temperature, we used the integrand of the line–luminosity per volume, effectively the first moment of the line–luminosity function. The shot power at a given redshift is proportional to the second moment of the line–luminosity function (see Equation 8 in Keating et al. (2016) for the full

relation including prefactors):

$$P_{\text{shot}}(z) \propto \int L^2 \phi(L) d(\log L) = \int L^2(M) \frac{dn}{d \log M} d(\log M). \quad (10)$$

We can calculate $L_{\text{line}}^2(M)dn/d(\log M)$ using the mean $L_{\text{line}}(M)$ relations for our models with $dn/d(\log M)$ from the same halo mass function fit from Behroozi et al. (2013b) that we used above for $dT/d(\log M)$. We then re-express this as dP_{shot}/dM to illustrate differential contributions to shot power from different halo mass ranges, in units of $\mu\text{K}^2 \text{Mpc}^3$. We show this in Figure 3 as well, along with the differential contributions to $\langle T_{\text{CO}} \rangle$ and $\langle T_{\text{HCN}} \rangle$.

Breaking down the brightness temperature in this way, we can see that the strict cutoff at $10^{10} M_{\odot}$ likely affects $\langle T_{\text{CO}} \rangle$ significantly in our implementation of the power-law model, but the effect is greatly diminished for $\langle T_{\text{HCN}} \rangle$ (as we anticipated in Section 2.2.3) to the point of being negligible. The CO temperature is also higher for the fiducial model because of the higher $L_{\text{CO}}(M)$ at $10^{12} M_{\odot}$ (as shown in Figure 1), around the knee of the fiducial halo mass–CO luminosity relation. However, the power-law model predicts a large contribution to $\langle T_{\text{HCN}} \rangle$ from high-mass emitters, which is not present in the turnaround model. We will return to these extreme emitters with halo mass $\gtrsim 10^{13} M_{\odot}$ in the power-law model as we discuss the rest of our results, and specifically to the illustration of shot noise contributions by halo mass in Section 3.2.

Given the above, we may attribute a substantial part of the temperature differences between the fiducial model and the power-law models to the form of the halo mass–SFR relation. Accordingly, variations on the fiducial HCN model through tweaking α and β in the $L_{\text{IR}}-L'_{\text{HCN}}$ relation do not result in differences as great. For $\alpha = 1.09$ and $\beta = 2.0$, following Carilli et al. (2005), $\langle T_{\text{HCN}} \rangle = 0.083^{+0.012}_{-0.009}$ (median and 95% sample interval). For $\alpha = 1.23$ and $\beta = 1.07$, following García-Burillo et al. (2012), $\langle T_{\text{HCN}} \rangle = 0.052^{+0.007}_{-0.005}$ (median and 95% sample interval).

3.2. Power spectra

Figure 4 depicts the 3D and 2D power spectra from our simulated data cubes for the fiducial model. On top of median spectrum values, we also show the amount of lightcone-to-lightcone variation that exists in the CO spectra including

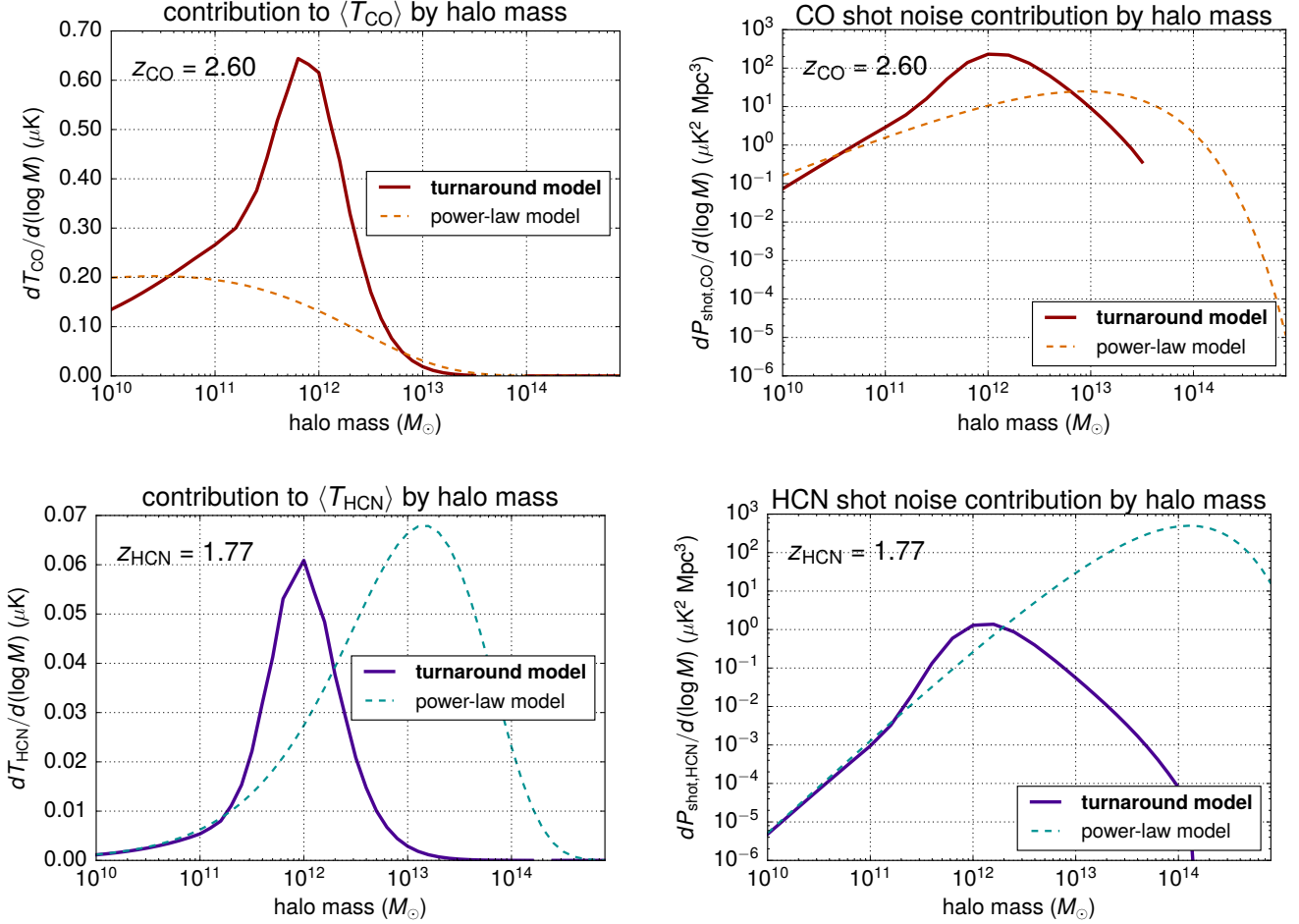


Figure 3. Expected contributions by halo mass to brightness temperature (**left panels**) and the shot noise component of the power spectrum (**right panels**), of CO emission at $z = 2.60$ (**upper panels**) and HCN emission at $z = 1.77$ (**lower panels**), for the fiducial turnaround model and the power-law model. We quantify the contribution from halo masses $M_{\text{vir}} \in [M, M + dM]$ to average temperature as $dT/d(\log M) \propto L_{\text{line}}(M) dn/d(\log M)$, and the contribution to the shot noise component as $dP_{\text{shot}}/d(\log M) \propto L_{\text{line}}^2(M) dn/d(\log M)$. Note that the y-axis limits differ between the upper left and lower left panels, but not the upper right and lower right panels. All calculations use the line-luminosity models in this work and the halo mass function fit from Behroozi et al. (2013b). As in Figure 1, the redshifts correspond to an observed frequency of 32 GHz for each line, at the midpoint of the simulated observing band.

contamination. For comparison, we also show $\Delta^2(k)$ values from COPSS as given in Keating et al. (2016), which was published during the preparation of this work. These data constitute the first and presently only detection of the CO autocorrelation spectrum signal at any spatial mode as far as we are aware.

For our fiducial model, the HCN spectrum lies well below the CO spectrum, by a few orders of magnitude. However, the model variations from Section 2.2.3 affect the HCN spectrum to varying degrees, as Figure 5 shows. Most notably, both of our power-law models place the HCN spectrum well above the CO spectrum, despite Section 3.1 showing lower average cube temperatures in HCN than in CO for all models. The bias introduced in the total line intensity power spectra is similar between $\Delta^2(k)$ and C_{ℓ} , although there is slightly less contamination in the former at the largest physical scales due to a stronger clustering signal. (This is to be expected—the survey volumes are elongated in the line-of-sight direction, so line-of-sight clustering ignored in the cube-averaged

C_{ℓ} contributes significantly to $P(k)$ at lower k .) Again, the power-law model has a different choice of IR–CO luminosity scaling that diminishes CO spectra in comparison to the fiducial spectra, but the relative rise in HCN spectra is due to no such thing. Spectrum contamination in the turnaround model is also possible if we increase log-scatter in HCN luminosity, although the median HCN spectrum even for $\sigma_{\text{HCN}} = 1.0$ dex is not as high as the CO spectrum for smaller k or ℓ .

Credible changes in the $L_{\text{IR}}-L'_{\text{HCN}}$ relation make little difference by comparison. Looking at the shot noise component of the power spectrum, the median $P_{\text{HCN}}(k = 1 \text{ Mpc}^{-1})$ over all simulated observations goes up by a factor of 1.5 relative to the fiducial model if we use $\alpha = 1.09$ and $\beta = 2.0$, following Carilli et al. (2005), and goes down by a factor of 2.2 relative to the fiducial model if we use $\alpha = 1.23$ and $\beta = 1.07$, following García-Burillo et al. (2012). While these are relatively small changes in comparison to the orders-of-magnitude changes going between turnaround and power-law models, they do show that the level of empirical uncer-

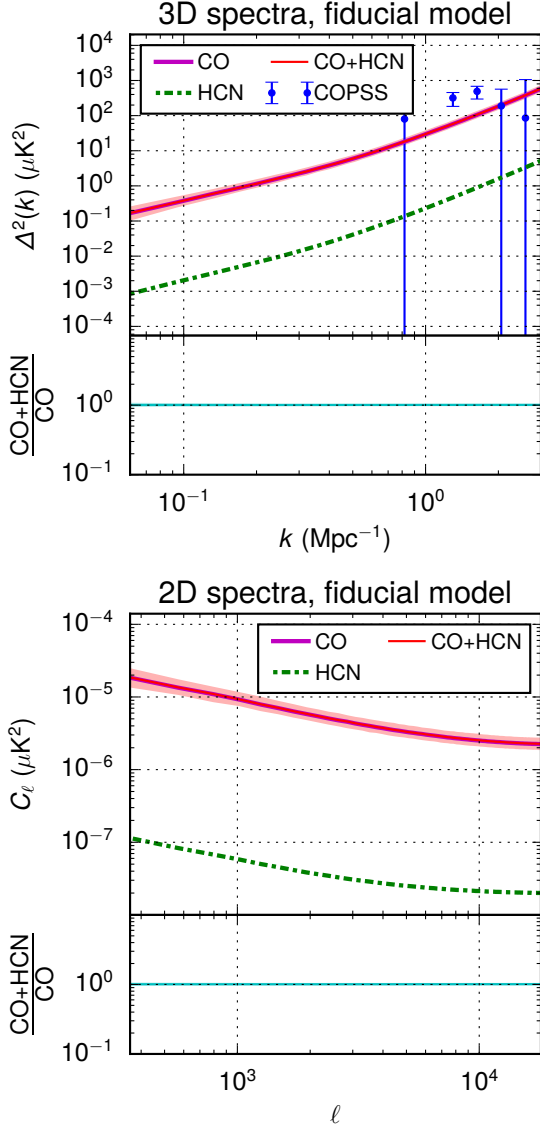


Figure 4. 3D spherically-averaged power spectra (**upper panel**) and average C_ℓ over all frequency channels (**lower panel**), for the fiducial model. Within each panel, the upper plot shows the auto spectrum for the CO signal only, the HCN contamination only, and the CO signal plus HCN contamination. Median spectrum values and 95% sample interval (the latter shown only for CO plus HCN) at each k or ℓ are shown for each model, with fractional residuals between uncontaminated and contaminated CO spectra shown below each spectra plot. We also show $\Delta^2(k)$ values from analysis of the full COPSS data set by Keating et al. (2016).

tainty in even the local IR–HCN connection alone implies a range of uncertainty of a factor of several in the HCN power spectrum.

For both high log-scatter and power-law models, the HCN spectrum is very flat across the different modes (i.e. C_ℓ and $P(k)$ are roughly constant, meaning $\Delta^2(k) \propto k^3$), and is entirely shot noise-dominated, unlike in the fiducial model. Again, Figure 3 analytically illustrates what bins of halo masses we expect to contribute most to this shot noise component of the signal. For the fiducial model, most of the shot noise for both CO and HCN comes from halos of mass

Table 4. Mean over all simulated observations of 496 lightcone pairs of total signal-to-noise ratio (SNR) for $P(k)$ over all modes.

Model	CO (no HCN)	CO + HCN
turnaround:		
$\sigma_{L_{\text{HCN}}} = 0.0$ dex	2.19	2.20
$\sigma_{L_{\text{HCN}}} = \mathbf{0.3}$ dex	2.19	2.20
$\sigma_{L_{\text{HCN}}} = 0.5$ dex	2.19	2.20
$\sigma_{L_{\text{HCN}}} = 1.0$ dex	2.19	2.29
power-law:		
f_{duty} of halos emit	1.17	6.97
all halos emit	0.64	1.38

NOTE—The fiducial model parameters are indicated in bold. Models are as described in the main text in Section 2.2.2, and in Table 3. SNR is given within the 30–34 GHz band, and per patch, not per survey.

$\sim 10^{12} M_\odot$, at the $L_{\text{line}}(M)$ downturn. However, in the power-law model, the shot power originates from much higher-mass halos: the differential shot power peaks around $10^{13} M_\odot$ for CO and around $10^{14} M_\odot$ for HCN (which has a steeper IR–line luminosity relation than CO). So as in Section 3.1, we find a class of extreme HCN emitters only in the power-law models, with profound implications for predicted power spectra. We will revisit this class of emitters in Section 3.4, where we examine differences in the numerically obtained HCN luminosity functions across these models.

3.3. Detection significance

We use the CO detection significance metric used in Li et al. (2016), which is the sum in quadrature of the signal-to-noise ratio (SNR) of $P(k)$ over all k :

$$\text{SNR}_{\text{total}}^2 = \sum_i \left[\frac{P(k_i)}{\sigma_P(k_i)} \right]^2, \quad (11)$$

where i indexes the binned spherical modes we obtain for $P(k)$. In their Appendix C, Li et al. (2016) outline the calculation of $\sigma_P(k)$, which incorporates Gaussian noise, sample variance from binning of the full $P(\mathbf{k})$ into shells, and resolution limits. (A beam size of $4'$ means that we effectively cannot meaningfully detect $P(k)$ beyond $k \sim 1 \text{ Mpc}^{-1}$, and for those modes $\sigma_P(k) \gg P(k)$. No beam smoothing is done in the cube, however.)

The extent to which HCN contamination biases detection significance varies greatly, mostly depending on whether we use a power-law model or the turnaround model; Table 4 gives the mean total SNR over all modes for each model variation, and evidently the power-law models predict far higher HCN contamination in total CO SNR. While the CO spectra are comparatively lower in those models, this is not the sole reason the SNR bias is so much greater. If we mix models and use CO cubes generated with the fiducial model but HCN cubes generated with the power-law model (with all halos emitting), then there is still significant contamination in SNR, which rises from 2.19 to 2.82—almost a 29% increase compared to the $\lesssim 1\%$ increase in the fiducial model. We em-

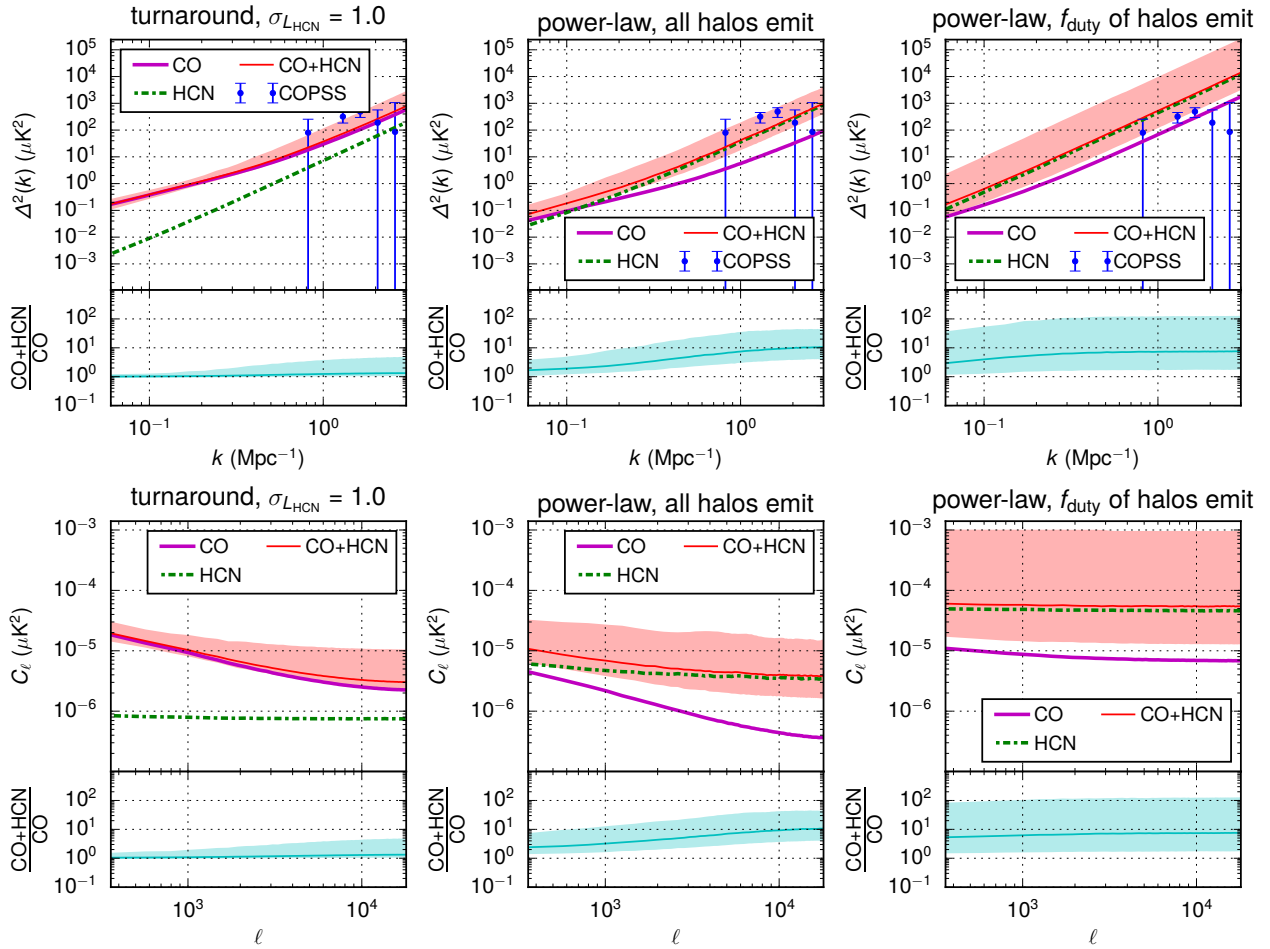


Figure 5. 3D spherically-averaged power spectra (**upper panels**) and average C_ℓ over all frequency channels (**lower panels**), for varied HCN line-luminosity models. Within each panel, the upper plot shows the auto spectrum for the CO signal only, the HCN contamination only, and the two combined. Median spectrum values and 95% sample interval (the latter shown only for CO plus HCN) at each k or ℓ are shown for each model, with fractional residuals between uncontaminated and contaminated CO spectra shown below each spectra plot. We again also show $\Delta^2(k)$ values from COPSS analysis by Keating et al. (2016).

phasize that these large increases are unlikely to be consistent with constraints on the galaxy–halo connection at high mass.

As with mean map temperatures in Section 3.1 and shot noise power spectra values in Section 3.2, varying the $L_{\text{IR}}-L'_{\text{HCN}}$ relation does not result in great differences, with the mean total SNR moving up from 2.19 to 2.21 following Carilli et al. (2005), or 2.20 following García-Burillo et al. (2012).

Li et al. (2016) give signal-to-noise for a survey of four identical patches, not for a single patch. Accounting for this plus the increased instrument bandwidth and finer spectral resolution in the current COMAP design, we still expect the initial phase of COMAP to reach an overall detection significance near Li et al. (2016)’s estimate of approximately 8σ .

3.4. Luminosity functions

To inform discussion of the above results, we present HCN luminosity functions for our simulated emitters.

Figure 6 shows the distribution of individual HCN luminosities as represented by the luminosity function $\phi(L)$, for a selection of models. (See Appendix B for details.) The

power-law models result in luminosity functions that appear to approximately follow a single power law or at least a smooth function, whereas the fiducial model appears to exhibit an exponential cutoff beyond a ‘knee’ of $L' \sim 10^9$ K km s $^{-1}$ pc 2 . Without a rapid cutoff in $\phi(L)$, the power-law models predict a significant population of extremely bright ($L'_{\text{HCN}} \gtrsim 10^{10}$ K km s $^{-1}$ pc 2), although still relatively rare, emitters—the same high-mass emitters shown in Figure 3 contributing a significant part of $\langle T_{\text{HCN}} \rangle$.⁴ The brightest HCN emitters would thus end up an order of magnitude brighter in our observations under those models than in our fiducial model. Variations on our fiducial model in α or β in the IR–line-luminosity relation (as discussed in Section 2.2.2 and mentioned earlier in this section) do not alter luminosities or temperatures anywhere nearly as much.

Increased log-scatter in HCN luminosity in the turnaround

⁴ The effect is not as drastic in CO, likely due to the higher α leading to lower-mass, lower-luminosity halos being more important in the first place. See Figure B2 for an illustration.

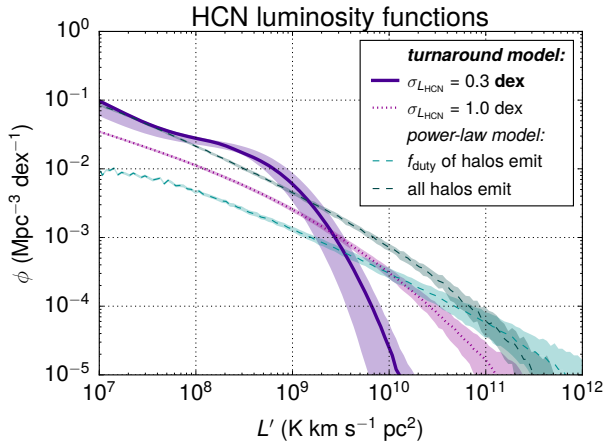


Figure 6. Luminosity function $\phi(L)$ for HCN for varied line-luminosity models. The fiducial HCN model (the turnaround model with 0.3 dex scatter in line-luminosity) does not produce a significant population of halos above $L' \sim 10^9$ K km s $^{-1}$ pc 2 , whereas the power-law models (plus the turnaround model with extremely broad 1.0 dex scatter in line-luminosity) do produce a population of such bright (if still rare) emitters. Median values and 95% sample intervals of $\phi(L)$ are depicted.

model also results in broader distributions of luminosities and temperatures. With 1.0 dex scatter, the resulting $\phi(L)$ for HCN is qualitatively similar to what we obtain from the power-law models. The $\phi(L)$ curve takes on a broader shape simply due to the increased variance in HCN luminosity from halo to halo at fixed halo mass. However, in the case of the power-law models, the $\phi(L)$ curve takes on a broader shape even when the duty cycle is assumed to be unity and all halos emit, i.e. without any halo-to-halo variance in HCN luminosity for a given halo mass. Therefore, the luminosity function varies by model both due to different halo-to-halo scatter in luminosity and due to the basic form of the mean halo mass–line-luminosity relation.

Note also that 1.0 dex scatter in the relation is so high that the correlations that our references claim would scarcely be observable. Even at high redshift, we have no reason to believe there would not be such an observable correlation.

4. DISCUSSION

4.1. Comparison with previous work

Breysse et al. (2015) provide our main point of comparison for line contamination forecasts, with simulated 2D maps of emission (for a single observing frequency) in a variety of lines, including CO and HCN. That work saw large simulation uncertainty due to variations in halo numbers and luminosities, but generally saw HCN spectra to be within an order of magnitude of CO spectra and found it to significantly affect observed power spectra, although no quantitative measure of this effect is provided. Since that work used 2D maps (550 deg 2 each), it uses C_ℓ to characterise the auto spectra in these maps at different scales, with ℓ ranging from 10^1 to $\gtrsim 10^3$. HCN amplitude begins to even exceed CO amplitude beyond $\ell \sim 10^3$.

Early single-dish surveys like COMAP, due to their small

survey field size, will probe a range of ℓ about an order of magnitude higher than the mock surveys of Breysse et al. (2015), at $\sim 10^2$ to $\sim 10^4$. The sensitivity of COPSS peaks at the upper end of this range. Thus, the effect of HCN contamination predicted by the power-law models, meant to mimic the model of Breysse et al. (2015), is even more striking. Yet in the results obtained with our fiducial turnaround model, the effect appears negligible, with the HCN auto spectra lying several orders of magnitude below CO spectra for all spatial modes, in both 2D and 3D data.

4.1.1. Lessons from model variations

Two factors influence the level of HCN contamination in our simulated observations.

1. Does the model incorporate the commonly expected fall-off in star-formation efficiency beyond halo masses of $\sim 10^{12} M_\odot$? If not—and if SFR, IR luminosity, and line-luminosities remain well-correlated at high mass and high redshift—a population of very bright, very sparsely distributed HCN emitters from intermediate redshift will overshadow the high-redshift CO signal.
2. How much stochasticity or scatter is in the halo mass–line-luminosity relation? If the galaxy population at intermediate redshift ends up with far more dramatic gas dynamics and time-evolution characteristics as a whole, we may expect extreme intrinsic scatter in line-luminosity in comparison to the high-redshift population. The resulting amount of scatter and thus shot noise in the HCN contamination could overpower the CO spectrum. However, this effect is subject to lightcone-to-lightcone sample variance, and not necessarily alarming in the context of an initial overall CO $P(k)$ detection at the scales that COMAP targets.

The first point is particularly relevant, as past work on line contaminants and often on line-intensity surveys in general—including Pullen et al. (2013) and Breysse et al. (2015)—have considered simpler linear or power-law halo mass–line-luminosity relations, much like the power-law models in this work. Some works like Gong et al. (2011) and Li et al. (2016) do incorporate a non-monotonic relation not described by a simple single power law. In fact, previous work supports a non-power-law relation between halo mass and SFR, as Behroozi et al. (2013a) note. Compared to the power-law models, the fiducial model also predicts lower HCN line-luminosities that tie more closely with HCN detections and upper limits at high redshift, as we discuss briefly in Appendix A.

The shape of the halo mass–HCN luminosity relation significantly affects the contribution of the high-mass halo population in simulated observations, and thus the conclusions drawn from those simulations. Predicted HCN spectra are higher with the power-law models compared to the fiducial model by several orders of magnitude, and when predicting bias in CO detection significance due to HCN contamination, power-law model predictions far exceed the fiducial predictions. As the luminosity functions in Section 3.4 demon-

strate, the power-law models result in more high-luminosity halos, which are still rare enough that their spatial distribution within each lightcone is quite sparse (see Figure 2 for a visual reference), and their statistics vary greatly from lightcone to lightcone. Thus, both 2D and 3D power spectra take on a flat shape and a wide 95% sample interval across repeated simulations, most of the spread being due to HCN rather than CO.

Note that the second factor—the amount of stochasticity or scatter present—includes the exact implementation of f_{duty} in the power-law models. Introducing a duty cycle of $f_{\text{duty}} \ll 1$, in particular, leads to extreme halo-to-halo scatter in line-luminosity, and thus to shot noise dominating the power spectrum for all molecular lines. However, we see similar differences between the fiducial models and the power-law models, with or without selecting only f_{duty} of halos—so f_{duty} is not solely responsible for the differences that we see.

4.1.2. Discrepancies against Breyse et al. (2015)

The results in this work and the results given by Breyse et al. (2015) diverge quantitatively, even with the same halo mass–line-luminosity models. Simulated observations generated via the power-law models have $\langle T_{\text{CO}} \rangle \approx 0.47 \mu\text{K}$ and $\langle T_{\text{HCN}} \rangle \approx 0.14 \mu\text{K}$, compared to predictions in Breyse et al. (2015) of $\langle T_{\text{CO}} \rangle \approx 0.60 \mu\text{K}$ and $\langle T_{\text{HCN}} \rangle \approx 0.023 \mu\text{K}$. Values of C_ℓ are also somewhat elevated relative to Breyse et al. (2015), at least at $\ell \sim 10^3$, where our range of ℓ overlaps with the range of ℓ in Breyse et al. (2015). Comparing between Figure 5 in this work and Figure 1 in Breyse et al. (2015), the contrast is more drastic for HCN than for CO.

We are still exploring reasons behind these discrepancies and what factors affect them. However, they likely arise from differences between the two works in halo mass cutoff, halo mass completeness, and halo mass function. We noted the first two of these in Section 2.2.3. Both are critical for an accurate simulation of CO emission, since lower-mass emitters can contribute non-negligibly to the CO signal. As we can see in Figure 3, our simulations lack some of these fainter emitters due to the strict mass cutoff of $10^{10} M_\odot$, and this contributes to the lower sky-averaged CO temperature in comparison to Breyse et al. (2015). Note also that the fiducial CO spectrum is somewhat lower than the COPSS measurements from Keating et al. (2016), which we could ascribe to missing faint CO emitters in our simulations.

Furthermore, even minor differences in the halo mass function will affect the power spectrum noticeably—particularly for HCN, as the choice of mass function in the approach of Breyse et al. (2015) would significantly impact the high-mass halo population. As discussed above, this population is small but a dominant influence in the HCN auto spectrum.

Broadly, our results for both of the power-law models are in line with Breyse et al. (2015): if we assume simple power-law halo mass–line-luminosity relations, we expect that the brightest HCN emitters raise HCN spectrum amplitudes to be on par with CO spectrum amplitudes on the spatial scales being observed, and expect significant contamination of CO spectra. However, we do not have high confidence in the power-law relations underlying these models, as discussed above.

4.2. Implications for CO surveys

For COMAP and other near-future surveys with a goal of initial CO signal detection, we find HCN contamination may not pose the most significant risk to such an initial detection. Under our fiducial model, the effect on total detection significance is sub-percent level. Given the uncertainty in relative intensities of CO and HCN, and the lack of data on the HCN luminosity function, we should not completely dismiss HCN as a possible contaminant. However, mitigation of HCN should be placed at a lower priority than mitigation of other systematics and astrophysical foregrounds.

The net effect of line contamination may be several times higher than forecast here—perhaps 5 to 10 percent in terms of relative bias in total CO $P(k)$ detection significance—once we incorporate consistent modelling of other lines, many of which we expect to have average luminosities similar to HCN. Breyse et al. (2015) consider a variety of line contaminants beyond HCN, including CN(1-0) and HCO+(1-0), emitting respectively at rest frequencies of 113 GHz and 89 GHz, close to CO(1-0) and HCN(1-0).⁵

However, all of these contaminant lines trace denser gas than CO, and emit at lower rest frequencies than CO(1-0). Both facts work to our advantage in a CO intensity mapping survey: much of our signal will come from aggregated fainter galaxies, where lower gas densities and the frequency-dependence of thermal emission enhance CO emission above denser tracers.

For far-future surveys at similar or higher redshifts, which may attempt to extract more sophisticated information about galaxy assembly and star-formation, the impact of HCN contamination could potentially be more marked. Higher angular resolution and instrumental sensitivity would ideally allow us to detect higher- k modes. However, the effect of HCN contamination in $\Delta^2(k)$ only worsens for higher- k modes in our simulated observations, for all models considered. Breyse et al. (2016) describe how such contamination affects inferences about the galaxy population based on voxel intensity distributions. For the more pessimistic models of HCN emission, we may expect similarly adverse effects on the inferences that Li et al. (2016) present, given the contamination we see in $\Delta^2(k)$.

Many future CO(1-0) intensity surveys will cross-correlate against other large-scale structure tracers, potentially including higher-order CO lines. While such analysis would exclude systematics and foregrounds not common to both data sets, they would not exclude molecular line foregrounds like HCN with their own higher-order lines. HCN(2-1)–HCN(1-0) contamination in a CO(2-1)–CO(1-0) survey would likely be of the same level of concern as HCN(1-0) in COMAP, since we expect the 2-1 and 1-0 lines to be of similar luminosity. (In their analysis of HCN detections, García-Burillo et al. (2012) adopt a line ratio of $L'_{\text{HCN}(2-1)}/L'_{\text{HCN}(1-0)} = 0.7$ from an empirical mean.) To best characterise the target and contaminant signals in isolation, we must cross-correlate

⁵ We expect HCO+ in particular to emit at luminosities similar to HCN, contrary to estimates shown in Breyse et al. (2015) at the time of writing.

against large-scale structure tracers beyond line-intensity surveys, such as QSO or galaxy surveys as explored in Pullen et al. (2013). As that paper suggests, a cross-correlation signal between such tracers and any molecular line—including HCN—would be of interest in its own right, although outside the scope of this study.

In the interim, our predictions for both target and contaminant signals will change, for better or worse. The results presented above use empirical models that build largely on observations of bright, local galaxies. Furthermore, these models build on a connection between star-formation activity and IR or line-luminosities, which is not entirely certain. Some or all of our current modelling may thus extrapolate poorly to faint galaxies or dwarf galaxies, and we must eventually move to physically motivated models of line-luminosity or spectral emission density templates to simulate line emission at high redshift in multiple lines simultaneously.

Changes in these predictions may come rapidly with advances in understanding of star-formation activity and its relation to molecular and dense gas. Such advances will arise not only from line-intensity surveys like COMAP, but also further observations of individual galaxies and clusters through ALMA and VLA, as well as the more recently commissioned *Argus* spectrometer at the Green Bank Observatory (Sieth et al. 2014).

5. CONCLUSIONS

Our primary conclusions are as follows:

- Under a basic power-law model, simulated HCN emission potentially seriously affects our CO power spectra and detection significance.
- However, in a more realistic model based on knowledge of high mass galaxies, we find that simulated HCN emission in a CO survey lies an order of magnitude below CO emission in temperature.
- The HCN auto spectrum also lies several orders of magnitude below the CO auto spectrum, across all spatial modes. The resulting contamination in total de-

tection significance is a small effect given reasonable amounts of halo-to-halo scatter.

Our fiducial model is somewhat better motivated than previous models, and predicts no serious contamination of CO power spectra. Still, we do caution restraint in dismissing HCN as a contaminant, given the limited observational information we have for high-redshift HCN(1-0) sources, and the plausibility of high intrinsic scatter at these redshifts. An investigation of high-redshift, high-mass halos hosting higher-luminosity ($L'_{\text{HCN}} \gtrsim 10^{10} \text{ K km s}^{-1} \text{ pc}^2$) HCN emitters would help constrain the duty cycle and luminosity scaling for HCN emission, which would refine future modelling.

In the run-up to surveys like COMAP, we expect further work on line contaminants, especially on the effect of such contamination on cross-correlation between complementary surveys, and the development of more sophisticated models and mitigation strategies for these contaminants. Indeed, during the preparation of this work, Lidz & Taylor (2016) and Cheng et al. (2016), working in the context of [CII] intensity surveys, have shown the possibility of separating strong CO line contamination from the targeted [CII] emission (at least at the power spectrum level), and even extracting useful information about both target and contaminant lines. While our expectation is that HCN contamination does not pose the greatest risk to CO intensity mapping, such techniques would readily find use in CO surveys if that expectation should change.

This work was supported by NSF AST-1517598 and by a seed grant from the Kavli Institute for Particle Astrophysics and Cosmology. We thank Patrick Breyse, Kieran Cleary, Andrew Harris, Brandon Hensley, and members of the COMAP collaboration, as well as an anonymous referee, for helpful discussions and comments. We thank Matthew Becker for providing access to the Chinchilla cosmological simulation (c400–2048) used in this work. This research made use of Astropy, a community-developed core Python package for astronomy (Astropy Collaboration et al. 2013), as well as Matplotlib (Hunter 2007) and a modified version of `hmf` (Murray et al. 2013). This research made use of NASA’s Astrophysics Data System Bibliographic Services. This work used computational resources at the SLAC National Accelerator Laboratory.

REFERENCES

- Astropy Collaboration, Robitaille, T. P., Tollerud, E. J., et al. 2013, *A&A*, 558, A33
- Behroozi, P. S., Wechsler, R. H., & Conroy, C. 2013a, *ApJL*, 762, L31
- , 2013b, *ApJ*, 770, 57
- Breyse, P. C., Kovetz, E. D., & Kamionkowski, M. 2015, *MNRAS*, 452, 3408
- , 2016, *MNRAS*, 457, L127
- Carilli, C. L., & Walter, F. 2013, *ARA&A*, 51, 105
- Carilli, C. L., Solomon, P., Vanden Bout, P., et al. 2005, *ApJ*, 618, 586
- Chang, T.-C., Pen, U.-L., Bandura, K., & Peterson, J. B. 2010, *Nature*, 466, 463
- Cheng, Y.-T., Chang, T.-C., Bock, J., Bradford, C. M., & Cooray, A. 2016, *ApJ*, 832, 165
- Chiang, L.-Y., & Chen, F.-F. 2012, *ApJ*, 751, 43
- Daddi, E., Dickinson, M., Morrison, G., et al. 2007, *ApJ*, 670, 156
- Decarli, R., Walter, F., Aravena, M., et al. 2016, *ApJ*, 833, 69
- Gao, Y., Carilli, C. L., Solomon, P. M., & Vanden Bout, P. A. 2007, *ApJL*, 660, L93
- Gao, Y., & Solomon, P. M. 2004, *ApJ*, 606, 271
- García-Burillo, S., Usero, A., Alonso-Herrero, A., et al. 2012, *A&A*, 539, A8
- Gong, Y., Cooray, A., Silva, M. B., Santos, M. G., & Lubin, P. 2011, *ApJL*, 728, L46
- Hunter, J. D. 2007, *Computing In Science & Engineering*, 9, 90
- Keating, G. K., Marrone, D. P., Bower, G. C., et al. 2016, *ApJ*, 830, 34
- Li, T. Y., Wechsler, R. H., Devaraj, K., & Church, S. E. 2016, *ApJ*, 817, 199

Table A1. Sample of high-redshift galaxies with HCN(1-0) detections or upper limits.

Source	z	lens mag.	L_{IR} ($10^{12} L_{\odot}$)	L'_{CO} ($10^9 \text{ K km s}^{-1} \text{ pc}^2$)	L'_{HCN}
VCV J1409+5628	2.583	1	17	74	6.5
APM 08279+5255	3.911	80	0.25	0.92	0.25
H1413/Cloverleaf	2.558	11	5.0	37	3.0
IRAS F10214+4724	2.286	17	3.4	6.5	1.2
J16359+6612(B)	2.517	22	0.93	3.7	0.6
BR 1202-0725	4.694	1	55	93	< 39.0
SMM J04135+1027	2.846	1.3	22	159	< 28.0
SMM J02399-0136	2.808	2.5	28	112	< 46.0
SDSS J1148+5251	6.419	1	20	25	< 9.3
SMM J02396-0134	1.062	2.5	6.1	19	< 3.7
SMM J14011+0252	2.565	25–5	0.7–3.7	4–18	< 0.3–1.5
MG0751+2716	3.200	17	2.7	9.3	< 0.9
RX J0911+0551	2.796	22	2.1	4.8	< 0.6

NOTE—Redshifts compiled in Solomon & Vanden Bout (2005) and luminosities compiled in Gao et al. (2007). All quantities are intrinsic, not apparent, and account for lens magnification as assumed in Gao et al. (2007). For SMM J14011+0252 we use the highest quoted values (assuming lowest lens magnification) for each luminosity in Figure A1.

Lidz, A., & Taylor, J. 2016, ApJ, 825, 143

Murray, S. G., Power, C., & Robotham, A. S. G. 2013, Astronomy and Computing, 3, 23

Noeske, K. G., Weiner, B. J., Faber, S. M., et al. 2007, ApJL, 660, L43

Pullen, A. R., Chang, T.-C., Doré, O., & Lidz, A. 2013, ApJ, 768, 15

Sieth, M., Devaraj, K., Voll, P., et al. 2014, Argus: a 16-pixel millimeter-wave spectrometer for the Green Bank Telescope, , , doi:10.1117/12.2055655

Solomon, P. M., & Vanden Bout, P. A. 2005, ARA&A, 43, 677

Sun, G., Moncelsi, L., Viero, M. P., et al. 2016, ArXiv e-prints, arXiv:1610.10095

Tekola, A. G., Berlind, A. A., & Väisänen, P. 2014, MNRAS, 439, 3033

Uzgil, B. D., Aguirre, J. E., Bradford, C. M., & Lidz, A. 2014, ApJ, 793, 116

Vallini, L., Gruppioni, C., Pozzi, F., Vignali, C., & Zamorani, G. 2016, MNRAS, 456, L40

Visbal, E., & Loeb, A. 2010, JCAP, 11, 016

Visbal, E., Trac, H., & Loeb, A. 2011, JCAP, 8, 10

Wang, R., Carilli, C. L., Neri, R., et al. 2010, ApJ, 714, 699

Wu, H.-Y., & Doré, O. 2017, MNRAS, 466, 4651

APPENDIX

A. OBSERVATIONAL CHECKS ON SIMULATED LINE-LUMINOSITY

Li et al. (2016) provide a brief comparison between the CO emission model in this work and observed CO luminosities, which showed general consistency. We attempt a similar comparison for our HCN models, but the sample of high-redshift HCN-emitting galaxies that we can use is much more limited, in number and in inferred properties. Unlike the references in Li et al. (2016), our references give no stellar masses for the galaxies observed, only gas masses and dust masses for some. Since we have no direct relation between halo mass and either of those masses, we will attempt only a very simple sanity check between our models and the observations available in the literature.

Table A1 shows a selection of high-redshift sources, as compiled in Solomon & Vanden Bout (2005) and Carilli & Walter (2013), for which Gao et al. (2007) (and references in each) give luminosities in IR, CO(1-0), and HCN(1-0). To compare these properties with what we expect from our models, we convert halo mass to the same luminosities as in Section 2.2.2, incorporating log-scatter in each relation. We consider a halo mass of $10^{13} M_{\odot}$, which is a probable halo mass size for LIRGs (Tekola et al. 2014), and also use a lower halo mass of $10^{12} M_{\odot}$. We then look at the scatter of the resulting sample predictions for both L'_{HCN} and L_{IR} or L'_{CO} , for a selection of high redshifts.

Figure A1 shows sample predictions over-plotted with the observations. We find that the HCN detections are broadly consistent with our model predictions, although the power-law model prediction is arguably overly bright if assuming a duty cycle of $f_{\text{duty}} \ll 1$ (see the cyan plus marker in the plots compared to the observed detections and upper limits, as well as the distributions of the fiducial predictions). Many detections are brighter in IR or line emission than the fiducial model predicts, but the fiducial model aims to describe relatively normal early-universe galaxies. By contrast, these detections are not only lensed (with magnifications of unspecified uncertainty), but also most analogous to extreme starbursts or ULIRGs, as Gao et al. (2007) note. It may be entirely reasonable to expect that in certain environments, as those experienced by starburst galaxies, the fall-off in star-formation efficiency may be slower or occur at higher mass than in other environments. Nonetheless, even though our models gloss over such factors in their simplicity, the predicted HCN luminosities for the input halo masses are essentially sane.

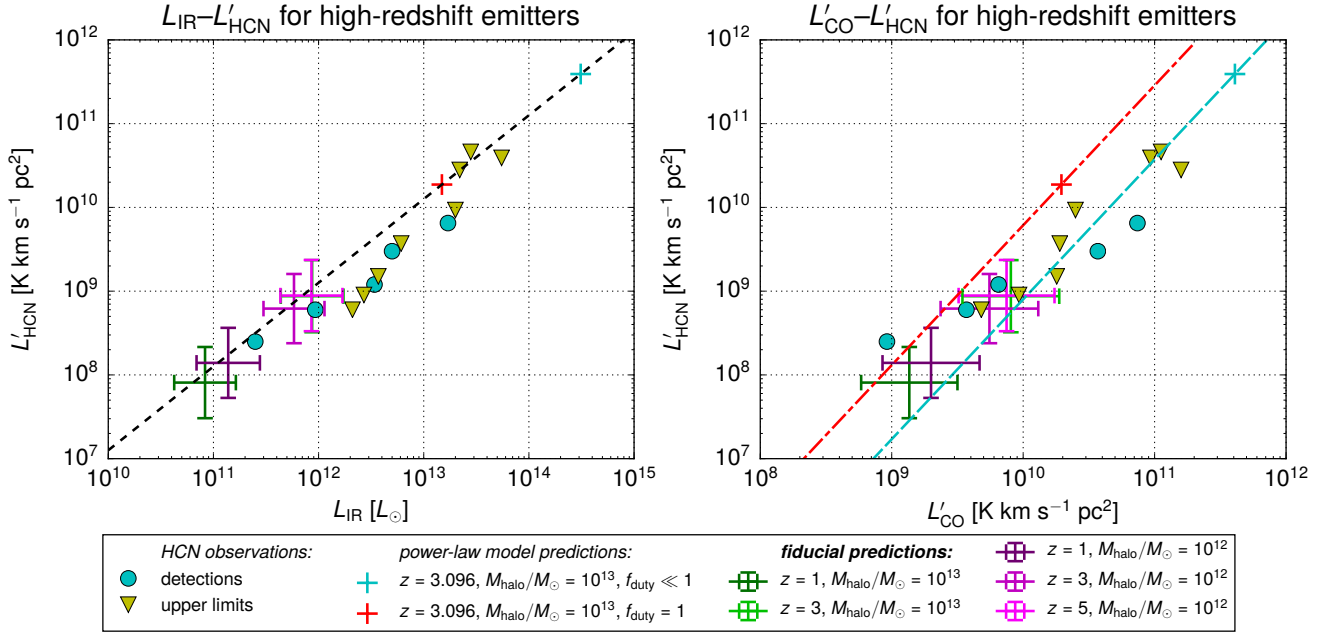


Figure A1. Predicted HCN line-luminosity against IR luminosity (**left**) and CO(1-0) luminosity (**right**), for a range of redshifts and halo masses (indicated in the plot legend). Error bars on fiducial predictions show marginal 1σ intervals for each luminosity. We base all luminosities on the fiducial models of Section 2.2.2. We over-plot observed HCN luminosities from Table A1 (cyan circles for detections, yellow triangles for upper limits). On the left panel, we over-plot the $L_{\text{IR}} - L'_{\text{HCN}}$ fit from Gao & Solomon (2004) (dashed line, black), used in both the power-law and turnaround models. On the right panel, we also plot the CO–HCN luminosity relation for the power-law model, both with $f_{\text{duty}} \ll 1$ absorbed into the luminosities and assuming a duty cycle of unity (dash-dotted line, red), and without it absorbed into the luminosities and assuming a duty cycle of f_{duty} (dashed line, cyan). We plot those relations only for $z = 3.096$, the mean redshift of the observed high-redshift sample.

Note that the halo mass is not directly observable for any of the high-redshift galaxies in Table A1, and we have assumed plausible halo masses for the purpose of this sanity check purely on theoretical grounds, without any firm observational basis. Adjusting these halo masses up or down by one or two orders of magnitude would drastically change our models’ luminosities. Thus we do not propose to either confirm or rule out any models with this sanity check, which merely shows that none of the models in this work assign outlandish luminosities to CO and HCN emitters. Additionally, we remind ourselves again that our models and more generally any of these ladders of observation- and simulation-based empirical relations are a decidedly primitive description of radio, sub-mm, and IR emission from dark matter halos.

We note the apparent scarcity of observations of HCN(1-0) emission in high redshift galaxies. The supplementary information for Carilli & Walter (2013) lists 61 detections of CO(1-0), but only 3 detections of HCN(1-0). These three were in the Cloverleaf, IRAS F10214+4724, and VCV J1409+5628 QSOs, with all three detections already compiled in Gao et al. (2007). Curiously, Carilli & Walter (2013) also lists no CO(1-0) detection for VCV J1409+5628, so we should not view its compilation of detections in the literature as complete by any means.

B. CALCULATION OF LUMINOSITY FUNCTIONS

As an extension of the work in Section 3.4, we present in Figure B2 both CO and HCN luminosity functions for individual halos (only down to $L' \sim 10^8$ K km s⁻¹ pc², to match results presented for CO(1-0) by Li et al. (2016), Keating et al. (2016), and others). We take counts of halos $N(L)$ in log-space luminosity bins ($L, 10^{\Delta(\log L)L}$), and calculate the luminosity function as

$$\phi(L) = \frac{N(L)}{\Delta(\log L) \Delta V}, \quad (\text{B1})$$

where ΔV is the lightcone comoving volume. Thus ϕ is number volume density per luminosity bin width, which is the typical definition of the luminosity function. Note the falloff and ringing of ϕ at extreme luminosity values (most visible for the power-law model with only f_{duty} of halos emitting), which is at least in part an artefact of the parameters of the simulation (the cutoff mass of $10^{10} M_{\odot}$ combined with the relatively high particle mass of the cosmological simulation).

Otherwise, the values for ϕ over the given range are not unreasonable for any of our models. While no space density data for HCN emitters appear to be available, the simulated CO luminosity function values for the models in this work do not compare unfavourably to data and fits that Vallini et al. (2016) and Decarli et al. (2016) present in the range of $L' \gtrsim 10^9$ K km s⁻¹ pc², where CO observational data are chiefly available. The overall features of the CO luminosity function, including the knee at $L'_{\text{CO}} \sim 10^{10}$ K km s⁻¹ pc², are entirely consistent with the 1σ constraints from COPSS data given in Keating et al. (2016).

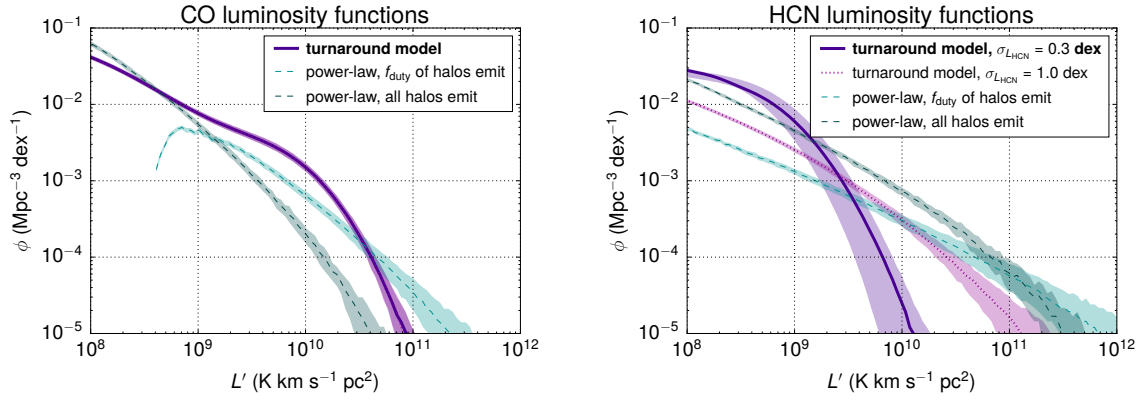


Figure B2. Luminosity function $\phi(L)$ for CO (**left panel**) and HCN (**right panel**) for varied line-luminosity models. The fiducial CO and HCN models carry 0.3 dex scatter in line-luminosity. For the turnaround model with $\sigma_{L_{\text{HCN}}} = 1.0$ dex, the HCN luminosity function is shown separately from the fiducial model's $\phi(L)$, but the change in HCN luminosity scatter does not (and should not) affect the CO luminosity function. Median values and 95% sample intervals of $\phi(L)$ are depicted.